Decomposition of the horizontal wind divergence associated with the Rossby, inertia-gravity, mixed Rossby-gravity and Kelvin waves on the sphere

Valentino Neduhal[1], Nedjeljka Žagar[1], Frank Lunkeit[1], Inna Polichtchouk[2], Žiga Zaplotnik[3]

[1]Meteorological Institute, Center for Earth System Research and Sustainability, Universität Hamburg, Germany
[2]European Centre for Medium-Range Weather Forecasts, Reading, UK
[3]Faculty of Mathematics and Physics, University of Ljubljana, Ljubljana, Slovenia

Key Points:

- A new method decomposes divergence due to the Kelvin, MRG, inertia-gravity (IG) and Rossby waves in terms of the zonal scales
- Up to about 6% of the zonally-integrated divergence power in the tropical UTLS in August 2018 in ERA5 is attributed to Kelvin and MRG waves
- Partitioning of the stratospheric divergence, almost entirely in IG waves, depends on the background flow

Corresponding author: Valentino Neduhal, valentino.neduhal@uni-hamburg.de

Abstract

The paper presents a new method for the decomposition of the horizontal wind divergence among the linear wave solutions on the sphere: inertia-gravity (IG), mixed Rossby-gravity (MRG), Kelvin and Rossby waves. The work is motivated by the need to quantify the vertical velocity and momentum fluxes in the tropics where the distinction between the Rossby and gravity regime, present in the extratropics, becomes obliterated. The new method decomposes divergence and its power spectra as a function of latitude and pressure level. Its application on ERA5 data in August 2018 reveals that the Kelvin and MRG waves made about 6% of the total divergence power in the upper troposphere within 10^0S-10^0N, that is about 25% of divergence. Their contribution at individual zonal wavenumbers k can be much larger; for example, Kelvin waves made up to 24% of divergence power at synoptic k in August 2018. The relatively small roles of the Kelvin and MRG waves in tropical divergence power are explained by decomposing their kinetic energies into rotational and divergent parts. The Rossby wave divergence power is 0.3-0.4% at most, implying up to 6% of global divergence due to the beta effect. The remaining divergence is about equipartitioned between the eastward- and westward-propagating IG modes in the upper troposphere, whereas the stratospheric partitioning depends on the background zonal flow. This work is a step towards a unified decomposition of the momentum fluxes that supports the coexistence of different wave species in the tropics in the same frequency and wavenumber bands.

Plain Language Summary

The atmosphere is commonly understood in terms of liner waves such as the large-scale, low-frequency and quasi-rotational Rossby waves and small-scale, high-frequency and quasi-divergent inertia-gravity (IG) waves. In extratropics, IG waves are commonly analysed in terms of the horizontal wind divergence. The same approach does not work in the tropics, where the Kelvin waves and mixed Rossby-gravity (MRG) waves hinder the frequency and scale separation as well as the separation between the vorticity and divergence. As a consequence, an assumption of a single wave type inhabiting a band of scales and frequencies is commonly made. We developed a method for the decomposition of divergence that does not require this assumption. By applying the new method to the ERA5 data in August 2018, we found that the Kelvin and MRG wave constituted up to approximately 25% of divergence in the tropical upper troposphere and lower stratosphere (UTLS). The remaining tropical divergence power is roughly evenly divided between eastward-propagating and westward-propagating IG modes in the upper troposphere whereas its partitioning in the tropical stratosphere and extratropics depends on the background zonal flow. Understanding divergence partitioning will lead to more accurate estimates of the vertical momentum fluxes in the UTLS.

1 Introduction

The divergence of the horizontal wind is a key variable of atmospheric general circulation, along with the vertical component of relative vorticity. Divergent winds and associated vertical motions drive variability from diurnal (e.g., Dai & Deser, 1999) to convective (e.g., Banacos & Schultz, 2005) and interannual and decadal time scales (e.g., Zurita-Gotor, 2019, 2021). Large-scale precipitation is often considered as a part of divergent circulation collocated with the maximal convergence such as monsoon (e.g., Trenberth et al., 2000) or the inter-tropical convergence zone (ITCZ; e.g., Berry & Reeder, 2014).

However, divergence remains uncertain, especially in the tropics where its amplitude relative to vorticity is largest. Divergence is the first order derivative of the wind and its accuracy is at best just as good as the wind observations. Large ocean areas of the tropics and the southern hemisphere are poorly covered by wind observations, leav-

ing the accuracy of divergent processes in these regions in reanalysis data to a large extent constrained by temperature information (i.e. satellite radiances), and model and data assimilation properties.

Indirect observations of the divergence field are possible using the Gauss's theorem applied to dropsondes distributed along circular flight patterns (Bony & Stevens, 2019, and references therein), an approach applied in the NARVAL2 (Bony & Stevens, 2019) and EUREC^{4}A (Bony et al., 2017) campaigns in the tropical Atlantic. While local and rare, such observations validate the divergence simulated by the km-scale models, in addition to elucidating process understanding. The comparison of the observed wind profiles during EUREC^{4}A with the model of the European Centre for Medium-Range Weather Forecasts (ECMWF) showed that the structure and variability of the trade winds are reasonably well reproduced by the model, although biases remain (Savazzi et al., 2022). Recently concluded Aeolus mission carrying the first Doppler wind lidar in space (Stoffelen et al., 2005) provided almost four years of global wind profiles that led to analysis and forecast improvements in all numerical weather prediction (NWP) systems that assimilated Aeolus winds (e.g., Rennie et al., 2021). The intercomparison of Aeolus data also quantified model biases in the upper tropical troposphere and lower stratosphere (UTLS) (Bley et al., 2022). However, the spatio-temporal scarcity and short duration of the Aeolus mission do not allow quantification of uncertainties in atmospheric divergence in weather and climate models. Consequently, divergence, or associated velocity potential, provided by (re)analyses is commonly used as a proxy of truth when analysing phenomena with significant vertical motions, from the large-scale flows such as the Walker circulation (e.g., Wang, 2002) to the organisation of convection and gravity wave dynamics (e.g., Uccellini & Koch, 1987). In fact, divergence is a common proxy of gravity or inertia-gravity (IG) waves (e.g., Waite & Snyder, 2009; Dörnbrack et al., 2022).

The spectrum of the kinetic energy associated with the divergent part of the horizontal circulation (i.e. the divergent kinetic energy as given by the Helmholtz decomposition) is one way to study gravity wave energetics (e.g., Waite & Snyder, 2009). This works well in extratropics thanks to large differences between the phase speeds and horizontal scales of the Rossby waves and gravity waves. The same approach breaks down near the equator where the Kelvin waves and the mixed Rossby-gravity (MRG) waves fill the frequency gap between the Rossby and gravity waves. Furthermore, tropical IG waves can have large scales and low frequency. Contributions of these non-Rossby waves (i.e. of the IG, MRG, and Kelvin waves) to the overall tropical divergence has not yet been performed. It is carried out in this paper which shows how divergence associated with the Kelvin, MRG and other waves vary with the zonal wavenumber, latitude and pressure level.

The NWP models and reanalysis systems which have dynamical cores based on the spherical harmonics as basis functions have divergence as a prognostic variable, for example, the ECMWF IFS model (e.g., Wedi, 2014). However, the spherical harmonics are eigensolutions of the linearised barotropic vorticity equation and are not informative about the tropical wave motions that are defined as eigensolutions of the linearised primitive equations on the sphere or on the equatorial beta plane (e.g., Matsuno, 1966; Gill, 1980; Kiladis et al., 2009; Webster, 2020). At small scales in the tropics, IG waves can be treated in the same way as in the midlatitudes, i.e. using the Boussinesq approximation and neglecting effects of rotation (e.g., Nappo, 2002). At synoptic and larger scales, the Kevin waves and the MRG waves become major contributors to the total non-Rossby wave variance spectra (Žagar et al., 2009a). The quantification of contributions of different wave species to the vertical momentum fluxes has so far assigned bands of wavenumbers and frequencies to a single wave type per band (e.g., Kim & Chun, 2015; Ern & Preusse, 2009). The work presented in this paper supports the presence of multiple waves in the same wavenumbers and frequency bands, a step towards a more realistic decomposition of the momentum fluxes driving the tropical middle atmosphere variability.

In what follows, we derive a unified method for the decomposition of divergence associated with the Kelvin, MRG, and IG waves, in addition to the Rossby waves. The method is spherical and provides the latitude-by-latitude and level-by-level divergence zonal wavenumber power spectra partitioned among the wave species. As stated above, we refer to the Kelvin, MRG, and IG waves, including their zonal-mean state (the zonal wavenumber $k = 0$), as the non-Rossby modes. As the Kelvin and MRG waves are equatorially trapped, the non-Rossby and IG modes are basically the same in the middle and high latitudes. Details of the method and its validation are provided in Section 2. Results of the method application to ERA5 reanalyses in August 2018 are presented in Section 3. Discussion, conclusions, and outlook are given in Section 4.

2 Decomposition of the horizontal wind divergence on the sphere

The decomposition of the horizontal wind divergence denoted $\mathcal{D}$, is derived using the normal-mode function (NMF) framework. The NMFs are the eigensolutions of the linearised primitive equations around the state of rest and they are defined as a product of the Hough harmonics and the vertical structure functions (VSFs) (e.g., Kasahara, 2020). First, the NMF decomposition is summarized in order to introduce the notation and variables. This is followed by the derivation of divergence and its zonal wavenumber spectra and the method validation.

2.1 The horizontal wind divergence in the NMF framework

The computation of divergence is carried out in the system with the pressure vertical coordinate. Starting from the adiabatic, hydrostatic primitive equations linearized about a motionless basic state on a flat Earth with the globally-averaged vertical temperature profile, one derives eigensolutions by making an assumption of separability between the vertical and horizontal dependencies. In this way, the global baroclinic atmosphere is represented in terms of M global shallow-water equation systems. The parameter M is defined by the number of the vertical layers used to discretize the atmosphere between the surface at pressure p_s and the top level where $p = 0$. Each shallow-water system is characterized by a mean depth, also known as the "equivalent depth", and it corresponds to one eigenvalue of the vertical structure equation (e.g., Staniforth et al., 1985). The equivalent depths couple the horizontal wind and geopotential height oscillations with the vertical structure functions - eigensolutions of the vertical structure equation. The horizontal motions are represented by a series of Hough harmonics which are products of the Hough vector functions in the meridional direction and waves in the longitudinal direction (Swarztrauber & Kasahara, 1985).

The 3D NMF decomposition consists of two steps. In the first step, the data vector $(u, v, h)^{\mathrm{T}}$ with the geopotential height (h) and two wind components (u, v) on the constant pressure levels is projected onto an orthogonal set of M vertical structure functions $G_m(p)$, $m = 1, .., M$. For a single point (λ, φ, p_j), the projection is written as

$$(u, v, h)^{\mathrm{T}}(\lambda, \varphi, p_j) = \sum_{m=1}^{M} G_m(p_j)\, \mathbf{S}_m\, (u_m, v_m, h_m)^{\mathrm{T}}(\lambda, \varphi) \ , \tag{1}$$

where the scaling matrix $\mathbf{S}_m$ is a 3×3 diagonal matrix with elements $\sqrt{gD_m}, \sqrt{gD_m}$ and D_m that make the data vector after the vertical projection, $(u_m, v_m, h_m)^{\mathrm{T}}$, dimensionless, denoted $(\tilde{u}_m, \tilde{v}_m, \tilde{h}_m)^{\mathrm{T}}$. Parameters λ and φ stand for the geographical longitude and latitude, respectively.

The non-dimensional rotating global shallow-water equations read

$$\frac{\partial \tilde{u}_m}{\partial \tilde{t}} - \sin\varphi\, \tilde{v}_m + \frac{\gamma_m}{\cos\varphi}\frac{\partial \tilde{h}_m}{\partial \lambda} = 0 \ , \tag{2a}$$

$$\frac{\partial \tilde{v}_m}{\partial \tilde{t}} + \sin\varphi\, \tilde{u}_m + \gamma_m \frac{\partial \tilde{h}_m}{\partial \varphi} = 0 \ , \tag{2b}$$

$$\frac{\partial \tilde{h}_m}{\partial \tilde{t}} + \frac{\gamma_m}{\cos\varphi}\left(\frac{\partial \tilde{u}_m}{\partial \lambda} + \frac{\partial}{\partial \varphi}(\tilde{v}_m \cos\varphi)\right) = 0 \ , \tag{2c}$$

where γ_m is a dimensionless parameter defined as $\gamma_m = \sqrt{gD_m}/(2a\Omega)$, with parameters D_m, a, Ω and g denoting the equivalent depth of the m-th vertical mode, the Earth radius, rotation rate, and gravity, respectively. The parameter γ_m is the inverse of the square of the Lamb's parameter which characterizes the nature of shallow-water flows (Swarztrauber & Kasahara, 1985). The discrete solutions of the system of equations (2) in terms of the Hough harmonics in space and harmonics in time can be written as

$$\begin{vmatrix} \tilde{u}_m\left(\lambda,\varphi,\tilde{t}\right) \\ \tilde{v}_m\left(\lambda,\varphi,\tilde{t}\right) \\ \tilde{h}_m\left(\lambda,\varphi,\tilde{t}\right) \end{vmatrix} = \sum_{n=1}^{R}\sum_{k=-K}^{K} \chi_n^k(m) \begin{vmatrix} U_n^k(\varphi;m) \\ \mathrm{i}V_n^k(\varphi;m) \\ Z_n^k(\varphi;m) \end{vmatrix} \mathrm{e}^{\mathrm{i}k\lambda}\mathrm{e}^{-\mathrm{i}\tilde{\nu}_n^k(m)\,\tilde{t}} \ . \tag{3}$$

The complex expansion coefficient $\chi_n^k(m)$ provides a multivariate spectral representation of the global 3D circulation, with a single mode defined by a unique index (k,n,m), with k and n defining the zonal wavenumber and the meridional mode index, respectively. For every vertical mode m in (1), the Hough harmonic $\mathbf{H}_n^k$ is defined as $\mathbf{H}_n^k\left(\lambda,\varphi;m\right) = \begin{vmatrix} U_n^k & \mathrm{i}V_n^k & Z_n^k \end{vmatrix}^{\mathrm{T}}(\varphi;m)\,\mathrm{e}^{\mathrm{i}k\lambda}$, where U_n^k, V_n^k and Z_n^k are the Hough functions for the zonal wind, meridional wind and the geopotential height, and the imaginary unit $\mathrm{i} = \sqrt{-1}$) in front of V_n^k accounts for its $\pi/2$ shift with respect to U_n^k (Swarztrauber & Kasahara, 1985). The Hough functions satisfy the energy norm

$$\int_{-1}^{1} (U_p U_r + V_p V_r + Z_p Z_r)\,\mathrm{d}\mu = \delta_{pr} \ , \tag{4}$$

where $\mu = \sin\varphi$, and p and r each represent a three-component modal index (k,n,m). Individual Hough harmonics $\mathbf{H}_n^k$ describe the horizontal structure of a single mode with $\tilde{\nu}_n^k(m)$ being the corresponding dimensionless frequency of that mode.

The mode index n includes 3 wave species: the westward-propagating Rossby modes and the eastward- and westward-propagating inertia-gravity modes, denoted EIG and WIG, respectively. Thus, the maximal number of meridional modes in (3), R, combines N_R Rossby modes including the mixed Rossby-gravity mode as the lowest meridional mode ($n = 0$) solution, N_{EIG} eastward-propagating inertia-gravity (EIG) modes, including the Kelvin waves as the lowest meridional mode ($n = 0$), and N_{WIG} westward-propagating inertia-gravity (WIG) modes; $R = N_R + N_{EIG} + N_{WIG}$. This particular choice of indexing is motivated by the wish to avoid another index going from 1 to 3 which would represent the three main wave species but would not support a separate treatment of the Kelvin and MRG modes. The notation (3) follows the NMF formulation in the MODES software (Žagar et al., 2015). Žagar et al. (2023) and references therein provides detailed discussion of the steps involved in the computation of $\chi_n^k(m)$.

The computations of divergence directly from the horizontal velocities expanded in terms of Hough harmonics (3) require the computation of the $\partial V_n^k/\partial\varphi$ that is not readily available but should be evaluated numerically. This makes the direct computation of divergence cumbersome. A natural way for computing $\mathcal{D}$ is to exploit the continuity equation (2c) as performed next. For vertical mode m, the non-dimensional divergence $\tilde{\mathcal{D}}_m$ can be expressed using Eq. (2c) as:

$$\tilde{\mathcal{D}}_m(\lambda,\varphi,\tilde{t}) = \tilde{\nabla}\cdot\tilde{\mathbf{V}} = -\frac{\partial}{\partial \tilde{t}}\tilde{h}_m(\lambda,\varphi,\tilde{t}) \, , \tag{5}$$

where the non-dimensional horizontal "del" operator is given by

$$\tilde{\nabla}_m = \frac{\gamma_m}{\cos(\varphi)}\Big[\frac{\partial}{\partial\lambda}()\,,\frac{\partial}{\partial\varphi}\Big(\cos(\varphi)()\Big)\Big]\,. \tag{6}$$

The spatial structure of the geopotential height for m-th vertical mode is given by the third equation in the equation set (3). Its substitution in (5) gives $\tilde{\mathcal{D}}_m$ as

$$\tilde{\mathcal{D}}_m(\lambda,\varphi,\tilde{t}) = \sum_{n=1}^{R}\sum_{k=-K}^{K} i\tilde{\nu}_n^k\,\chi_n^k(m)\,Z_n^k(\varphi)\mathrm{e}^{\mathrm{i}k\lambda}\mathrm{e}^{-\mathrm{i}\tilde{\nu}_n^k\tilde{t}}\,. \tag{7}$$

Analogous to (1), dimensional divergence at pressure level p is obtained by multiplying (7) with 2Ω and summing up contributions from all VSFs. Dropping the time dependence, divergence is defined as

$$\mathcal{D}\,(\lambda,\varphi,p) = \sum_{m=1}^{M}\sum_{n=1}^{R}\sum_{k=-K}^{K} \mathrm{i}2\Omega\tilde{\nu}_n^k(m)\,\chi_n^k(m)\,Z_n^k\,(\varphi;m)\;G_m(p)\,\mathrm{e}^{\mathrm{i}k\lambda}\,. \tag{8}$$

The major advantage of Eq. (8) is that $\mathcal{D}$ is obtained by a simple multiplication and summation over readily available VSFs and the Hough functions. All input coefficients and functions required in (8) are available after the expansion of 3D data such as using MODES. The divergence associated with the Rossby, IG, MRG, or Kelvin waves is obtained by limiting the summation to a subset of n associated with the modes of interest. Similarly, filtering in terms of the zonal wavenumbers is trivial. Žagar et al. (2023) make use of Eq. (8) in the derivation of the pressure vertical velocity ω and its kinetic energy spectra in the hydrostatic atmosphere.

Equation (8) states that divergence $\mathcal{D}$ has a phase shift of $\pi/2$ with respect to the geopotential height h. This is illustrated in Fig. 1 for several modes with the zonal wavenumber $k = 1$. For the eastward-propagating Kelvin and $n = 1$ EIG mode ($\nu > 0$), and for the westward-propagating $n = 1$ Rossby, $n = 0$ and $n = 1$ WIG and MRG waves ($\nu < 0$), divergence lags the geopotential height for the quarter of a cycle. The $\pi/2$ shift between the geopotential and divergence is an important universal property well known from the quasi-geostrophic theory for the Rossby waves (e.g., Holton, 2004), and from the polarization equations coupling the pressure, temperature, and velocity perturbations for internal gravity waves (e.g., Nappo, 2002). The same phase shift applies to the vertical velocity as $\mathcal{D}$ and ω are always in phase (Žagar et al., 2023).

2.2 Computation of the divergence power spectrum

An advantage of computing divergence in Hough harmonics space is the ease with which the associated zonal wavenumber power spectra can be computed. The Fourier expansion of divergence along the latitude circle is

$$\mathcal{D}\,(\lambda,\varphi,p) = \sum_{k=-K}^{K}\hat{\mathcal{D}}_k\,(\varphi,p)\,\mathrm{e}^{\mathrm{i}k\lambda}\,, \tag{9}$$

which combined with Eq. (8) gives the definition of the Fourier expansion coefficient $\hat{\mathcal{D}}_k$ as

$$\hat{\mathcal{D}}_k\,(\varphi,p) = \sum_{m=1}^{M}\sum_{n=1}^{R}\mathrm{i}2\Omega\tilde{\nu}_n^k(m)\,\chi_n^k(m)\,Z_n^k\,(\varphi;m)\;G_m(p)\,. \tag{10}$$

The Parseval theorem provides the total power of divergence on pressure level p along the latitude circle φ:

$$\frac{1}{2\pi}\int_0^{2\pi}\mathcal{D}^2\mathrm{d}\lambda = \sum_{k=-K}^{K}\hat{\mathcal{D}}_k\left[\hat{\mathcal{D}}_k\right]^* = \sum_{k=0}^{K}(2-\delta_{k0})\left|\hat{\mathcal{D}}_k\right|^2 = \sum_{k=0}^{K}E_D^k(\varphi,p) = E_D(\varphi,p)\,, \tag{11}$$

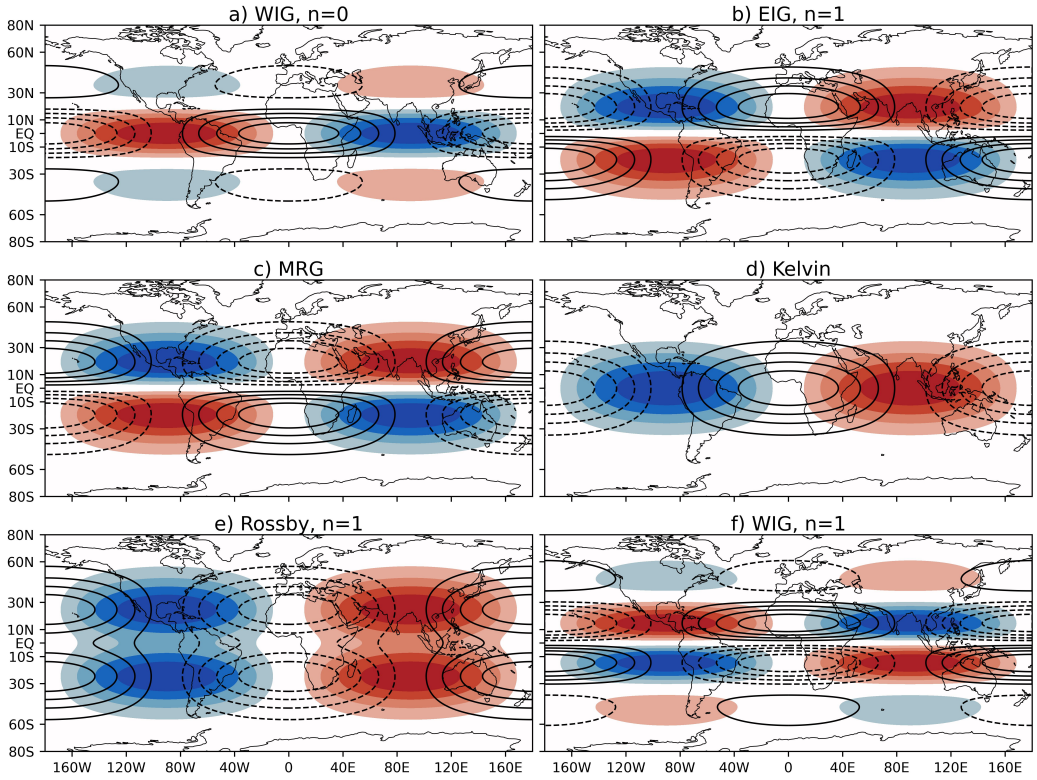

Figure 1. The horizontal structure of the geopotential height (colors) and divergence (isolines) for a) $n = 0$ westward inertia-gravity (WIG), b) $n = 1$ eastward inertia-gravity (EIG), c) mixed Rossby-gravity (MRG), d) Kelvin, e) $n = 1$ Rossby and f) $n = 1$ WIG mode for zonal wavenumber $k = 1$ and equivalent depth $D = 1015$ m. Blue colors and dashed lines denote negative geopotential height and convergence, respectively. Every field is normalized by its maximal values and the $[-1, 1]$ interval is shown with 0.2 spacing.

where $\delta_{k0} = 1$ for $k = 0$ and 0 otherwise (with $\hat{\mathcal{D}}_k$ presented only for $k > 0$). A single latitude circle divergence power spectra can be integrated meridionally on the Gaussian latitude grid used for the Hough harmonics expansion. For the latitude belt $[\varphi_1, \varphi_2]$, the total divergence power in zonal wavenumber k is

$$E_D^k(p) = \int_{\varphi_1}^{\varphi_2} E_D^k(\varphi, p)\, \cos\varphi \, \mathrm{d}\varphi \Big/ \int_{\varphi_1}^{\varphi_2} \cos\varphi \, \mathrm{d}\varphi \tag{12}$$

For $\varphi_1 = -\pi/2$ and $\varphi_1 = \pi/2$, we obtain the globally integrated divergence power spectrum $E_D^k(p)$. An example is shown in Fig. 2 for the global spectra averaged over stratospheric levels of ERA5 between 1 and 10 hPa and for the levels between 100 and 100 hPa.

The global divergence power spectra can be compared with the divergent kinetic energy of the horizontal wind (denoted E_{HD}) for the same dataset in Fig. 2 in order to highlight differences between the two types of spectra. The E_{HD} spectra as a function of the zonal wavenumber are computed by the spherical harmonics decomposition (e.g., Lambert, 1984; Adams & Swarztrauber, 2001) as

$$E_H^k = \frac{1}{4} \sum_{l=k}^{N} (2 - \delta_{k0})\, \frac{a^2}{l(l+1)} \left(|\hat{\zeta}_{l,k}|^2 + |\hat{\delta}_{l,k}|^2 \right) = E_{HR}^k + E_{HD}^k \,, \tag{13}$$

where l is the total wavenumber, N is the global truncation and $\hat{\zeta}_{l,k}$ and $\hat{\delta}_{l,k}$ are wave components of vorticity and divergence, respectively. The rotational (E^k_{HR}) and divergent (E^k_{HD}) kinetic energy spectra are widely used to compare kinetic energy distributions of weather and climate models with expected theoretical power laws and observations (e.g., Burgess et al., 2013; Skamarock et al., 2014; Wedi, 2014). Note that E^k_H spectra are usually presented in terms of the total wavenumber l, meaning that contributions from all $-l < k < l$ are included in the summation of energy in single l. A complementary way defined by Eq. (13) sums up all l contributing to a single zonal wavenumber in a triangular truncation decomposition. The summation involves weighted divergence expansion coefficients $\hat{\delta}_{l,k}$ by a factor $l(l+1)$ which comes from the spherical Laplacian of the meridional expansion in terms of the Legendre polynomials and the use of the Helmholtz decomposition (Adams & Swarztrauber, 2001).

The E^k_D and E^k_{HD} spectra are quantitatively and qualitatively different as seen in Fig. 2; they have different physical units and amplitudes and exhibit different spectral slopes and peaks. The E^k_D spectra describe the variance distribution of divergence $\mathcal{D}$ in a signal processing sense. The power peak at wavenumber k implies k with a dominant amplitude in the divergence field. In contrast, the E^k_{HD} spectra are not informative about the relative distribution of divergence in terms of k. More important, the Hough harmonics decomposition provides latitude-by-latitude spectra that shows anisotropy of spherical divergence, besides the wave decomposition.

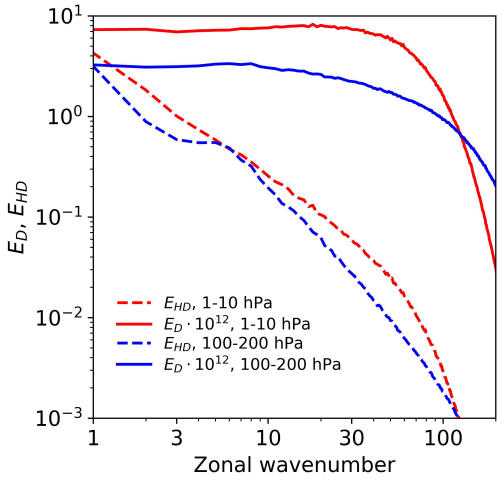

Figure 2. The divergent component of the horizontal kinetic energy spectra E^k_{HD} (in m^2 s^{-2}) computed using the spherical harmonic decomposition of the horizontal winds and globally integrated divergence power spectra E^k_D (in s^{-2}). Input data are ERA5 analyses in August 2018. The divergence power spectra are multiplied by 10^{12}.

The contributions of various wave species to the total divergence power at different wavenumbers can be quantified by taking the ratio between the spectral power $E^k_D(i)$ of wave species i with the sum of the powers of all five wave species at the same k:

$$R^k(i) = \frac{E^k_D(i)}{\sum_j E^k_D(j)}\,, \tag{14}$$

where $j = R, EIG, WIG, K, MRG$ and Rossby, Kelvin and MRG modes are denoted R, K and MRG respectively. Note that the contributions of various wave species to E^k_D

are not additive, in contrast to modal components of the mechanical energy that is derived using the energy norm (4) (Kasahara, 2020). The purpose of definition (14) is that the sum of individual contributions to the total divergent power is 1. Equation (14) thus provides a qualitative measure of how much various wave species contribute to the total divergence power. We checked that the effect of replacing the denominator of (14) by the total divergence E_D^k is not large (not shown).

Equation (10) suggests that the divergence power spectrum is proportional to the square of modal frequency $\nu(k,n,m)$, $E_D^k \propto \left[\nu_n^k(m)\right]^2$, that is, that the shapes of divergence power spectra for different waves are coupled to their dispersion relationships. Figure 3 shows the non-dimensional modal frequencies as a function of the zonal wavenumber for three equivalent depths and several meridional modes. It can be seen that the frequencies of the IG modes with small n get less dependent on k as the equivalent depth decreases. Frequency dependencies on k of different waves are discussed in Žagar et al. (2023) for the sphere, midlatitude and equatorial β planes. For the Kelvin and IG modes $\nu \propto k$, whereas for the Rossby and MRG modes $\nu \propto k^{-1}$. This implies much steeper divergence power zonal wavenumber spectra for the Rossby and MRG waves as can be expected given their rotational nature.

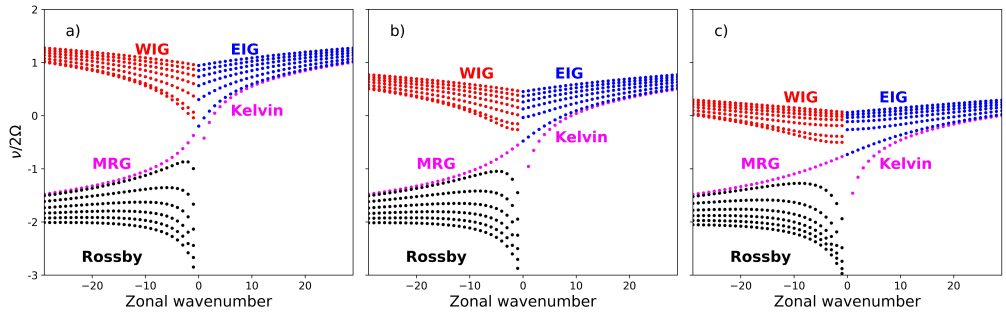

Figure 3. Frequencies of the normal modes for equivalent depths of approximately a) $D = 10$ km, b) $D = 1$ km, and c) $D = 100$ m. Frequencies are normalized by 2Ω and shown in a logarithmic scale. Frequencies of the eastward propagating inertia-gravity (EIG) are shown for the meridional indices $n = 1$, 5, 10, 15, 20, 25, where $n = 0$ EIG modes are Kelvin waves. Frequencies of the westward propagating inertia-gravity (WIG) are shown for the meridional indices $n = 0$, 1, 5, 10, 15, 20, 25 while Rossby modes are shown for the meridional indices $n = 1$, 5, 10, 15, 20, 25, where $n = 0$ Rossby modes are mixed Rossby-gravity (MRG) waves.

2.3 Data

The above described computation of the horizontal divergence in the pressure system is implemented in the MODES software (Žagar et al., 2015). The new module can be executed in a self-standing mode including scale-selected filtering of divergence in physical space. It is also a part of the procedure for the computation of the pressure vertical velocity as well as the vertical momentum fluxes.

As input fields, we are using ERA5 data (Hersbach et al., 2020). The IFS model, which is used to produce ERA5, has a 'sponge layer' near the model top to prevent spurious wave reflection. This sponge layer is scale-selective and directly damps divergence. The sponge layer is represented by adding a fourth-order hyper-diffusion (∇^4) to the prognostic equations for vorticity, divergence and temperature fields above 10 hPa to damp

vertically propagating waves with an e-folding time on a given total wavenumber l of

$$\left(\frac{L_{max}(L_{max}+1)}{l(l+1)}\right)^2 \frac{\tau_H}{1+7.5(3-\log(p))},$$

where L_{max} is the maximum total wavenumber 639 for ERA5, p is pressure in Pa, and τ_H is a timescale of 4320 s (1.2 hours). This hyper-diffusion is quite weak and has a small impact on the resolved waves. In addition, a first-order diffusion (∇) is applied on the divergence field above 1 hPa with an e-folding time on a given total wavenumber l of

$$\sqrt{\frac{L_{max}(L_{max}+1)}{l(l+1)}}\frac{\tau_H}{16-lev},$$

where $lev = 1, ..., 15$ is a vertical level index with $lev = 15$ corresponding to 1 hPa and $lev = 1$ corresponding to the model top. This diffusion is very strong and very effective at damping all resolved waves. Therefore, any analysis of divergence in the mesosphere, above 1 hPa, will be dominated by the spurious sponge effects and should be interpreted with caution. The detrimental impact of the IFS sponge layer on resolved gravity waves has been discussed by Gisinger et al. (2022) and Gupta et al. (2021).

At a horizontal grid spacing of about 30 km, with added effects from grid-scale hyperdiffusion, ERA5 skilfully resolves waves with a horizontal wavelength longer than about 200 km outside the sponge layer and parametrizes the rest. The unresolved part of the gravity wave spectrum is parameterized using the Lott and Miller (1997) scheme for orographic waves and the Orr et al. (2010) scheme for the non-orographic GWs. Moreover, the vertical diffusion parametrization, represented by the eddy-diffusivity mass-flux framework, acts in the stratosphere in ERA5.

The input data are defined on the 137 model levels. The list of levels can be seen at `https://confluence.ecmwf.int/display/UDOC/L137+model+level+definitions`. In order to keep the vertical resolution of the reanalysis data, the wind components and model-level geopotential are interpolated from the hybrid sigma-pressure levels to pressure levels corresponding to the globally averaged pressure of the full model levels. The interpolation method follows the method implemented in the ECMWF IFS system. The horizontal grid is a regular N320 Gaussian grid with 1280×640 points along the latitude circle and pole to pole, respectively, corresponding to a resolution of 31 km at the equator. The regular Gaussian grid data are extracted directly from the ECMWF MARS database (C3S, 2017) using the MIR interpolation procedure. For validating purposes, we analysed a few dates in August 2016 during the NARVAL campaign. The main dataset is for August 2018 that was used in Žagar et al. (2023) making possible a comparison between the spectra of the vertical kinetic energy and divergence.

The truncations used in MODES are $K = 350$ zonal wavenumbers, $R = 600$ meridional modes including $N_R = N_{EIG} = N_{WIG} = 200$ and $M = 60$ vertical modes. As the number of vertical modes is less than half of the number of levels, we expect significant deviations in $\mathcal{D}$ reconstructed by MODES from the divergence field extracted directly from ERA5. The reason for using a smaller number of vertical modes is a fast decrease in the equivalent depth that leads to equatorially-trapped horizontal structures (Žagar et al., 2009b). However, differences in the upper troposphere and in the middle atmosphere, which are the focus of our discussion, are not large or detrimental to the study. Except for a high-resolution NMF decomposition by Terasaki et al. (2011) that provided global energy spectra including 750 zonal wavenumbers, this is the highest resolution data analysed to date with MODES.

2.4 Method validation

Figure 4 compares divergence in ERA5 with its modal reconstruction $\mathcal{D}$ over the tropical Atlantic on 19 August 2016. The ERA model-level divergence is interpolated

to the same pressure levels as used in MODES. We picked a weather-rich day of 19 August with tropical storm Fiona (Kimberlain, 2016) as the hardest test for the method. The divergence associated with the storm can be seen near 18°N, 43°W throughout the troposphere. Modal $\mathcal{D}$ resembles ERA5 very well. Differences in the vertical cross-section through the troposphere are expected due to the vertical truncation. Detailed statistical evaluation of differences confirms that differences start below the level where the vertical decomposition is no longer complete (not shown).

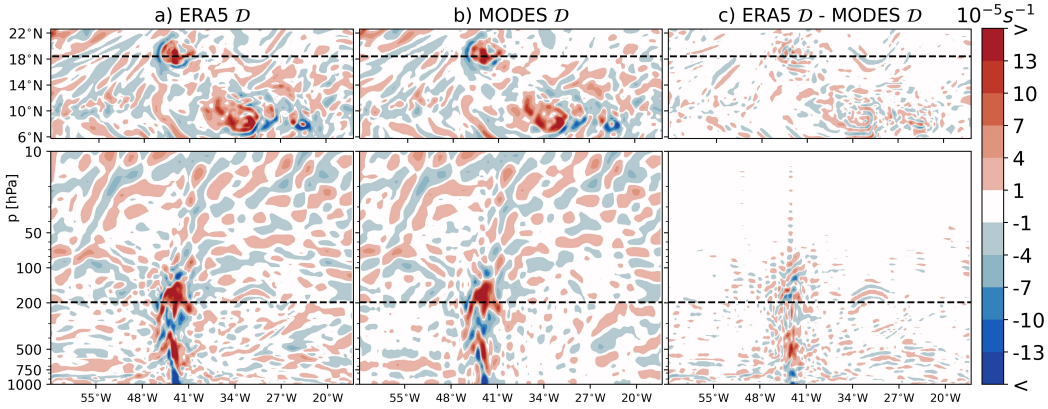

Figure 4. a) ERA5 divergence, b) divergence reconstructed by MODES and c) ERA5−MODES, at 10 UTC on 19 August 2016 at 197 hPa (top row), and the vertical cross-section along 18.4°N (bottom row). The dashed line in the top row is along 18.4°N and the dashed line in the bottom row indicates 197 hPa level.

In Fig. 5 the total divergence signal at 10 UTC on 19 August 2016 is decomposed into components and presented for the global domain at 150 hPa level. Although several panels in this figure appear very similar, this is the first example of the systematic decomposition of divergence and all components are presented for completeness. First, the total divergence $\mathcal{D}$ is separated into Rossby modes ($\mathcal{D}_R$) and non-Rossby modes ($\mathcal{D}_{nR}$), $\mathcal{D} = \mathcal{D}_R + \mathcal{D}_{nR}$. Then, $\mathcal{D}_{nR}$ is partitioned in terms of the IG modes ($\mathcal{D}_{IG}$), Kelvin modes ($\mathcal{D}_K$) and MRG modes ($\mathcal{D}_{MRG}$), $\mathcal{D}_{nD} = \mathcal{D}_{IG} + \mathcal{D}_K + \mathcal{D}_{MRG}$. Finally, IG modes are split into WIG and EIG parts, $\mathcal{D}_{IG} = \mathcal{D}_{EIG} + \mathcal{D}_{WIG}$. First of all, Fig. 5 shows that the global divergence is dominated by small scales and it nearly completely projects onto the IG modes. The WIG modes dominate in the extratropics where $\mathcal{D}_{WIG}$ is due to ageostrophic circulation associated with baroclinic Rossby waves superimposed on the mean westerly flow, especially in the Southern Hemisphere (SH) that has winter season (Fig. 5h). The divergence due to the linear Rossby waves is the geostrophic wind divergence on the sphere which is proportional to $v_g\,\beta/f$, has a small amplitude and a large-scale structure (Fig. 5b).

Focusing now on the tropics, we can notice a local maximum of the divergence in $\mathcal{D}_{IG}$, $\mathcal{D}_{EIG}$, and $\mathcal{D}_{WIG}$ due to the tropical storm Fiona discussed in Fig. 4. This is because the flow in cyclostrophic balance, typical for tropical cyclones (e.g., Jakobsen & Madsen, 2004), will in linear decomposition project partly on Rossby and partly on IG modes. Local maxima and minima in $\mathcal{D}_{IG}$ can be spotted along the inter-tropical convergence zone and in the monsoon-affected areas of South-East Asia and western Pacific, but also over the topographic gravity wave hot spot over the Andes, Himalayas, and the mid-west USA. The Kelvin wave divergence is centered at the equator and an order of magnitude smaller than $\mathcal{D}_{IG}$ with the largest scale and amplitudes over the Indian Ocean and West Pacific (Fig. 5d). In contrast, the MRG divergence, $\mathcal{D}_{MRG}$ (Fig. 5e), has a smaller amplitude and larger scales, similar to $\mathcal{D}_R$. Note also that $\mathcal{D}_{MRG} = 0$ at the equator where its zonal wind is zero and the meridional wind is strongest. This implies that the

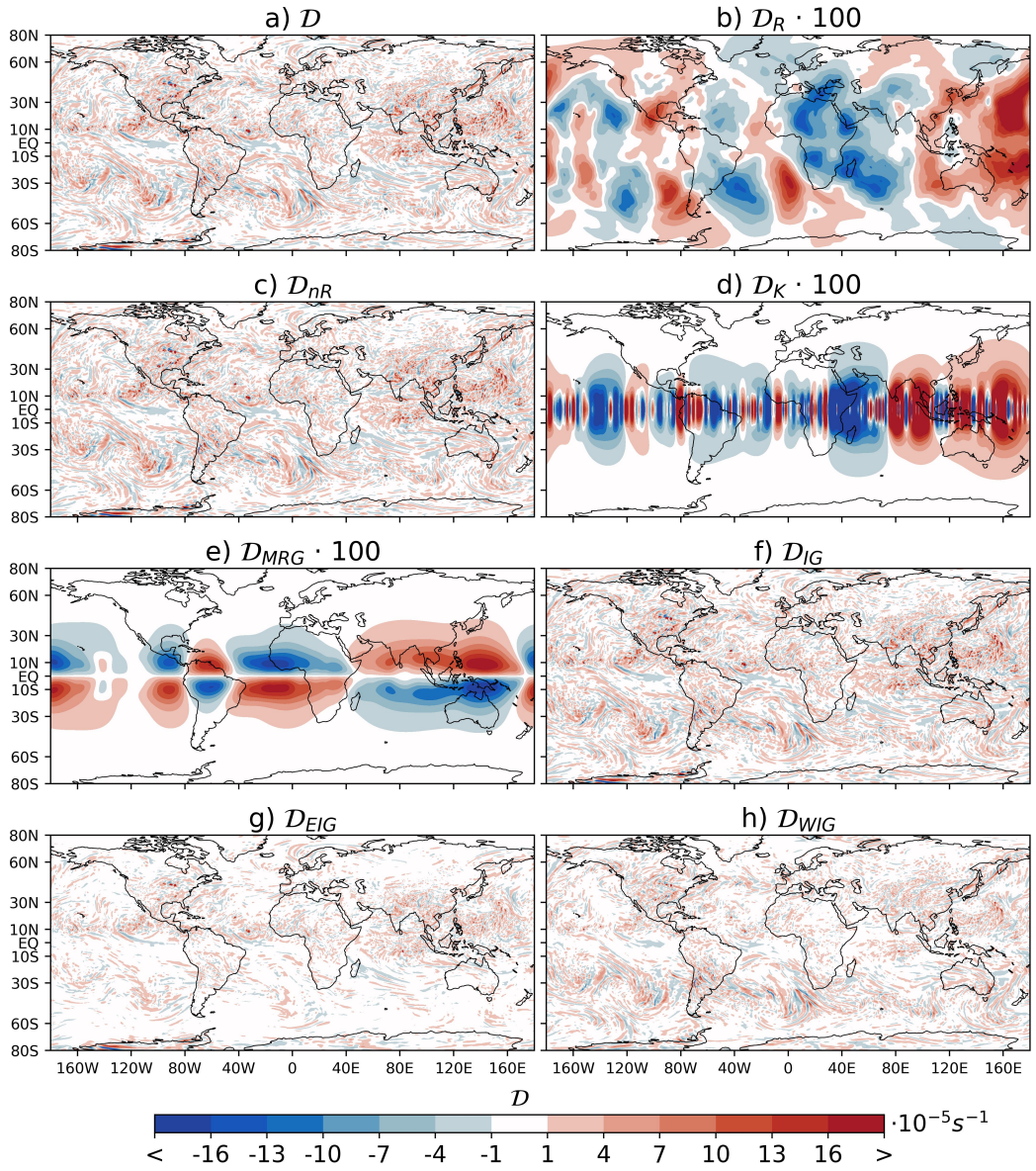

Figure 5. Total divergence $\mathcal{D}$, decomposed into the Rossby, $\mathcal{D}_R$, and non-Rossby, $\mathcal{D}_{nR}$, parts. The non-Rossby divergence is a sum of the Kelvin, $\mathcal{D}_K$, MRG, $\mathcal{D}_M$, and IG, $\mathcal{D}_G$, components, with $\mathcal{D}_G$ made of the EIG, $\mathcal{D}_{EG}$, and WIG, $\mathcal{D}_{WG}$, parts. The decomposition is applied to ERA5 circulation at the level near 150 hPa on 19 August 2016, 10 UTC. The Rossby, Kelvin and MRG parts are multiplied by 100.

vertical velocity and the vertical momentum fluxes of the MRG waves are also zero at the equator and likely to maximise within $5° - 10°$ degrees away from the equator.

Further comparison of divergence profiles over the NARVAL campaign region with $\mathcal{D}$ shows that ERA5 lacks many details in the vertical divergence profile and further details are missed by our incomplete reconstructions in the lower troposphere, although the main features and amplitude of the divergence profiles are represented reasonably

well. The $\mathcal{D}$ decomposition into components shows that the divergence is completely in the $\mathcal{D}_{IG}$ component as expected (not shown).

3 Modal decomposition of divergence in August 2018

Now we present level-by-level divergence power spectra in August 2018 for different latitude belts focusing on the upper troposphere and the middle atmosphere. The period was characterised by easterly zonal winds in the tropical stratosphere between the tropopause and about 20 hPa, i.e. the easterly phase of the Quasi-Biennial-Oscillation (QBO, e.g., Baldwin et al. (2001)) with strongest mean-zonal winds of about 50 m/s near 30 hPa. The strongest westerlies around 30 m/s were near 15 hPa, and easterlies were present above 5 hPa. The rest of the zonal mean flow was typical for this period of the year: prevalent weak easterlies in the tropical troposphere, westerlies in the SH, subtropics and middle latitudes, and a polar night jet in the middle atmosphere of SH high latitudes.

Even though we are primarily interested in the quantification of tropical divergence, it is worth presenting global properties of divergence spectra partitioned into the Rossby and non-Rossby parts as the first application of the new method. The results are split between the tropical, subtropical, midlatitude and high latitude belts for levels above 500 hPa. First, we discuss E_D^k in the middle and high latitudes, then the tropical spectra presented for every level after averaging over 31 samples. The shortest analysed scales appear noisy, most likely because of a short dataset. A longer dataset and the whole ERA5 periods are planned for the future work along with introducing the non-linear normal-mode decomposition to differentiate between slowly evolving IG modes slaved to the Rossby mode dynamics and faster IG modes including internal gravity waves (e.g., Ko et al., 1981; Tribbia, 2020).

3.1 Middle and high latitudes

Figure 6 and Figure 7 present the divergence power spectra E_D^k averaged over latitudes within $30°-60°$ and $60°-80°$ in both hemispheres, respectively. The Rossby E_D^k is multiplied by 100 in order to be visualised using the same colorbar as other components.

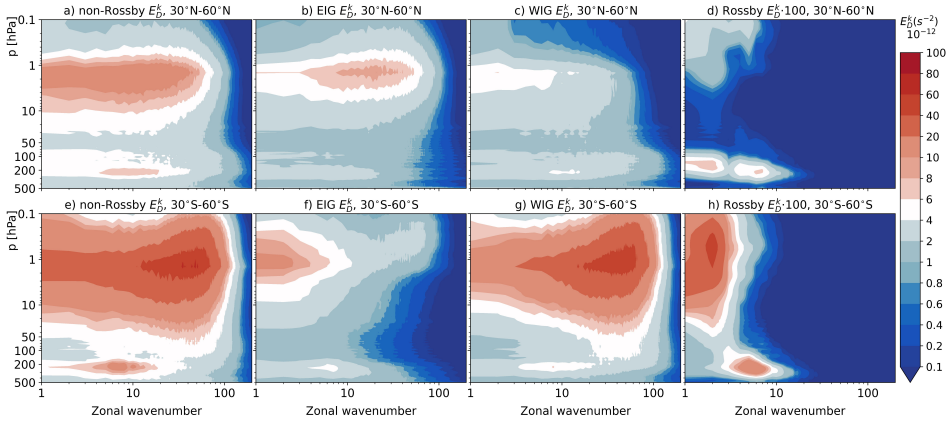

Figure 6. Level-by-level (a,e) non-Rossby, (b,f) EIG, (c,g) WIG and (d,h) Rossby mode divergence power spectra E_D^k averaged for latitude belts (a-d) $30°\text{N}-60°\text{N}$ and (e-h) $30°\text{S}-60°\text{S}$ for August 2018. The extratropical non-Rossby spectra correspond to the sum of WIG and EIG spectra. The Rossby spectra are multiplied by 100. Note the nonlinear contour intervals.

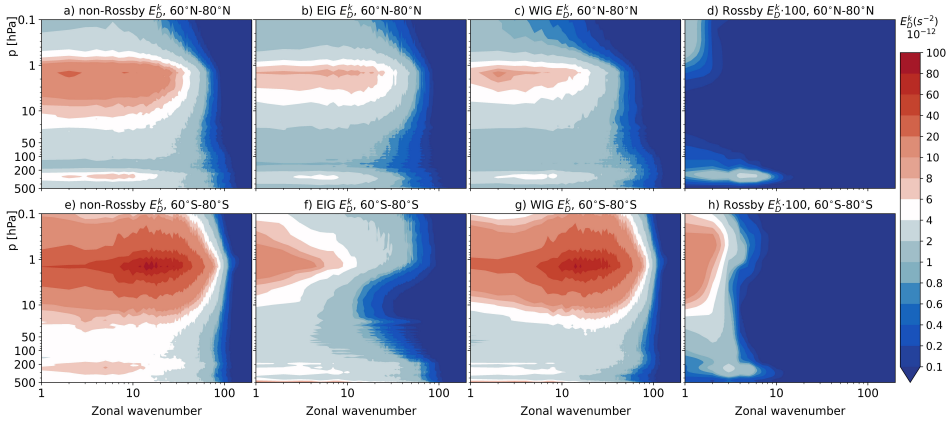

Figure 7. As in Fig. 7 but for (a-d) 60°N−80°N and (e-h) 60°S−80°S.

A prominent feature of the two figures is the maximum in stratospheric E_D^k near 1 hPa at subsynoptic scales of IG modes. While present in both hemispheres, it is predominantly in the WIG divergent spectra of the winter hemisphere (SH), with the maximum at $k \approx 50$. The maximal E_D^k in the Northern Hemisphere (NH) is smaller and shifted to larger scale compared to the SH.

The E_D^k maximum near 1 hPa is due to the artificial sponge layer in ERA5, which very strongly damps divergence from 1 hPa upwards (see section 2.3) and therefore leads to all gravity waves depositing their momentum at or near the 1 hPa level (see e.g., Fig. 2c in Gupta et al. (2021)). If the sponge layer was absent, the maximum would be located at a much higher altitude, at a natural breaking/saturation level of gravity waves (cf. Fig. 2c to Fig. 2d in Gupta et al. (2021)). A decrease in the divergence power of IG modes for $k > 100$ is due to the insufficient resolution of the ERA5 data. In IFS model simulations at higher horizontal resolution than ERA5, the small-scale gravity waves with $k > 100$ play an increasingly important role in the momentum budget (Figs. 2 and 3 in Polichtchouk et al. (2023)).

The majority of mesoscale E_D^k in WIG modes in extratropical winter hemisphere (SH) can be understood by vertically-propagating IG waves filtered by the westerly flow of the stratospheric polar vortex (Fig. 6g and Fig. 7g). Such features can be seen in the real-time decomposition of the ECMWF forecasts on the MODES webpage, `https://modes.cen.uni-hamburg.de/products#POL`. A significant level of divergence power at planetary scales in panels e), f), and g) of Figs 6-7 is most likely due to the linear mode decomposition. The linear balance decomposition of the polar vortex, which is characterised by the gradient wind balance, partially projects the vortex onto the planetary-scale IG modes, and in our case mainly onto the WIG modes as the basis functions are derived for the state of rest. When the linear modal decomposition will be replaced by the non-linear decomposition (Ko et al., 1981), the planetary-scale divergence, now in IG modes, should become a part of the balanced flow providing an easier interpretation of the remaining IG modes as unbalanced flow.

The Rossby wave E_D^k is 2-3 orders of magnitude smaller than the IG E_D^k at the same levels and scales. The Rossby E_D^k peaks across the stratopause at $k = 2$ in midlatitudes (Fig. 6h) and at $k = 1$ in high latitudes of the winter hemisphere (SH) (Fig. 7h). Even though the peak extends well above 1 hPa, it is possibly affected by the artificial sponge layer in ERA5. There is a strong vertical gradient in the Rossby E_D^k amplitudes in the upper stratosphere (Fig. 6h and Fig. 7h), associated with the Rossby wave attenuation as they propagate upward in the winter stratosphere (e.g., Charney & Drazin, 1961). In

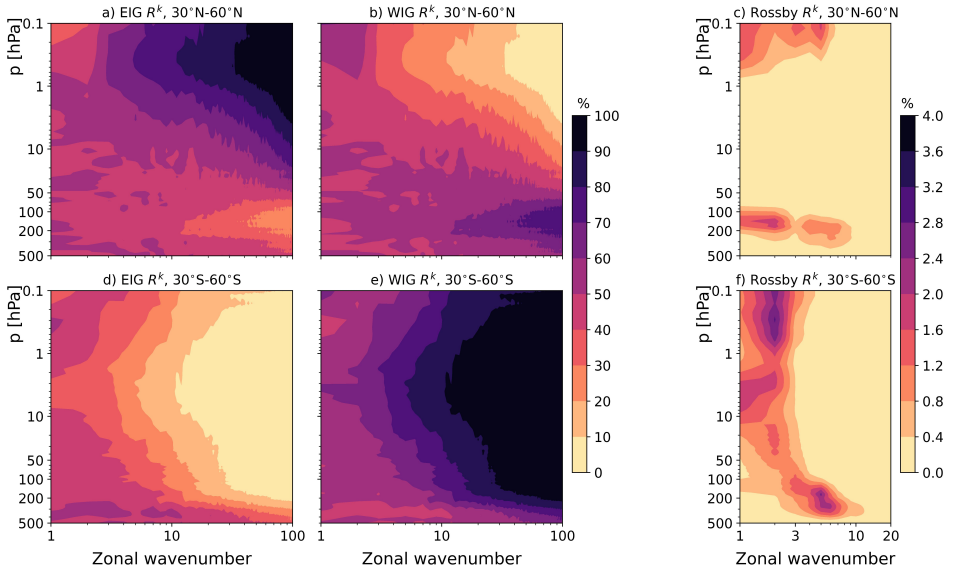

Figure 8. Relative contribution to E_D^k by the (a,d) EIG, (b,e) WIG and (c,f) Rossby modes in the latitude belt (a-c) 30°N−60°N and (d-f) 30°S−60°S.

the troposphere, a secondary maximum in the Rossby E_D^k at synoptic scales in midlatitudes can be seen near 300 hPa, with a stronger peak in the winter hemisphere. An increased signal at the same levels and scales is present also in the non-Rossby E_D^k spectra (Fig. 6e) that can be coupled with ageostrophic circulation and inertia-gravity waves excited by jets and baroclinic processes (e.g., O'Sullivan & Dunkerton, 1995; Plougonven & Zhang, 2014).

How large is the contribution of the IG modes to divergent power at different levels and scales? This can be quantified by evaluating Eq. (14) and the result is presented in Fig. 8 for the two midlatitude belts. It shows that the stratospheric mesoscale divergence power in the winter hemisphere is up to 90% due to WIG modes because of the filtering effect of the background flow (Fig. 8d-e). A small part is due to the planetary Rossby waves, 3-4% at most at $k = 5{-}10$ in the upper troposphere and at $k = 1, 2$ in the upper stratosphere (Fig. 8f). Similarly, due to middle atmosphere easterlies in the summer hemisphere (NH), the mesoscale E_D^k above 10 hPa is up to 90% EIG (Fig. 8a). Lower down in the upper troposphere and across the tropopause layer, EIG and WIG modes contribute about equally to divergence power reflecting no direction preference for mesoscale gravity waves and divergence sources in the troposphere. The higher latitudes (not shown) have % very similar to midlatitudes but with the maximal contribution of Rossby modes at $k = 1$ near 1 hPa and making less than 1% of total E_D^k (not shown).

3.2 Tropics and Subtropics

The tropical divergence power spectra are presented in Fig. 9. While overall similar to extratropical spectra, maxima in tropical non-Rossby E_D^k spectra extends from synoptic to planetary scales in the upper troposphere (Fig. 9a vs. Fig. 6a). This is a signature of the large-scale non-Rossby waves including the Kelvin and MRG waves in the upper tropical atmosphere (e.g., Wheeler et al., 2000; Yang et al., 2003; Žagar et al., 2009a; Kiladis et al., 2009, 2016), known to drive middle atmosphere processes such as the QBO.

Divergence defines the vertical velocity which in turn defines the vertical momentum fluxes (e.g., Baldwin et al., 2001; Lu et al., 2020).

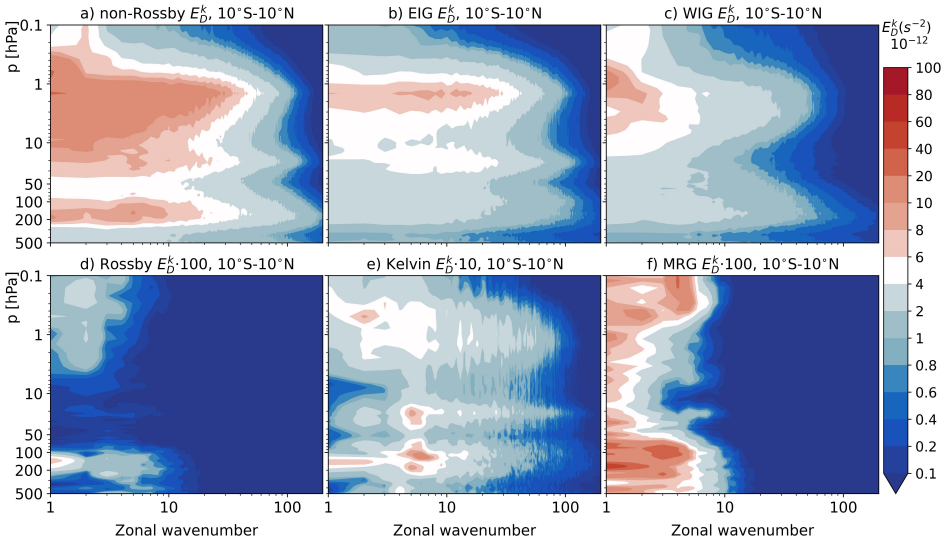

Figure 9. Level-by-level (a) non-Rossby, (b) EIG, (c) WIG, (d) Rossby, (e) Kelvin and (f) MRG mode divergence power spectra E_D^k averaged within 10°N−10°S. The Rossby and MRG spectra are multiplied by 100, and the Kelvin wave spectrum is multiplied by 10. Note the non-linear contour intervals.

The decomposition of the non-Rossby divergence into the four wave types provides scale- and altitude-dependent differences between the Kelvin and MRG waves and the IG modes. The vertical distributions of E_D^k are expected to be strongly coupled with the shear lines of the zonal-mean zonal flow that is therefore included in Fig. 10 which shows relative power in the five wave species. Transitions between easterlies and westerlies explain differences between the EIG and WIG E_D^k and their relative contributions to the total divergence power spectrum. It shows that the EIG exceeds the WIG E_D^k at sub-synoptic scales in the stratosphere (Fig. 9b vs. Fig. 9c and Fig. 10a vs. Fig. 10b), especially in the layer with westerly shear around 30 hPa. Both EIG and WIG signals maximize near 1 hPa (Fig. 9b,c), most likely due to the sponge layer, but at different scales: the WIG E_D^k has the largest amplitude at $k = 1{-}3$ whereas a broad maximum of EIG E_D^k is centered around $k = 10$ that corresponds to wavelength of about 2000 km. In the upper troposphere without strong shear lines in the mean zonal flow, EIG and WIG modes have more similar contributions to E_D^k. The Rossby mode divergence power in August 2018 was at least two orders of magnitudes smaller than non-Rossby E_D^k everywhere except at $k = 1$ near 150 hPa (Fig. 9d). The Rossby E_D^k makes no more than 1.2% of E_D^k at $k = 1$ between 100-200 hPa (Fig. 10c), whereas nearly everywhere else in wave space it is below 0.5%.

There is a large difference between the IG and the Kelvin and MRG mode divergence in both amplitudes and scale selection of the signals (Fig. 9e,f). First of all, the Kelvin wave divergence power in August 2018 was an order of magnitude greater than the MRG E_D^k. The Kelvin wave signal peaks at several synoptic-scale wavenumbers in the upper troposphere and there is a secondary peak at $k = 1$ within the tropopause layer (Fig. 9e). At these wavenumbers, the Kelvin E_D^k makes up to about 25% of the total divergence power (Fig. 10d). For the MRG waves, the E_D^k spectra are more flat at large scales with little signal beyond $k = 10$ in the UTLS region (Fig. 9f). The MRG

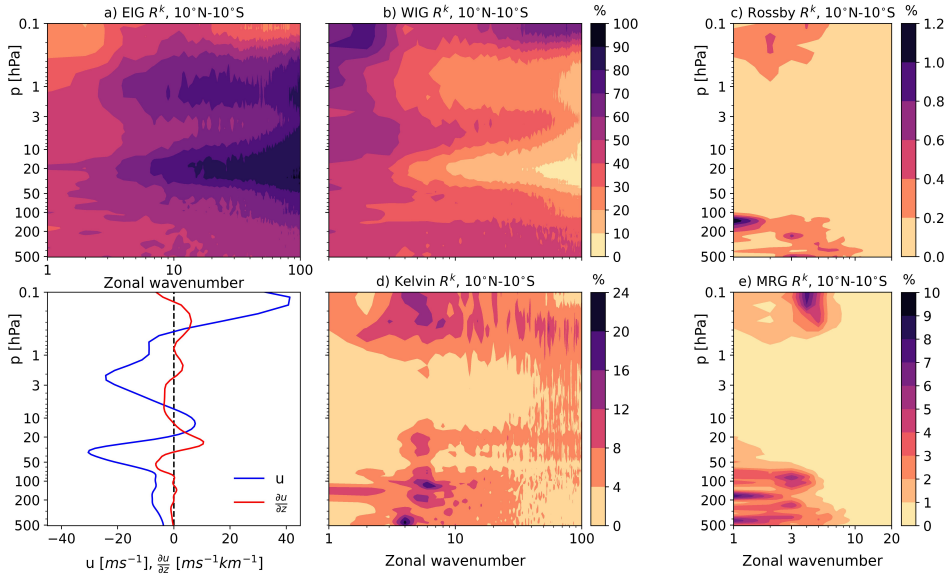

Figure 10. Relative contribution to E_D^k by (a) EIG, (b) WIG, (c) Rossby, (d) Kelvin and (e) MRG modes in the tropical belt 10°N−10°S. The additional panel shows the profile of the zonal mean zonal wind u and its shear as $\partial u/\partial z$.

contribution to the total E_D^k at individual wavenumbers in August 2018 does not exceed 10% which is twice smaller than for the Kelvin waves.

The five E_D^k spectra are additionally shown in Fig. 11 for two tropical layers to compare the spectral slopes of E_D^k for various wave species with respect to their frequencies discussed in Section 2. The two layers are the 100-200 hPa layer with the maximal divergence in the upper troposphere and the 20-30 hPa layer with the maximal westerly shear in the stratosphere. Figure 11a shows dominance of EIG over WIG E_D^k in the layer where the WIG waves likely meet the critical levels. The EIG E_D^k spectra are nearly white or have a slightly positive slope over a range of $k \approx 5 - 50$. The WIG and EIG E_D^k spectra are more similar within the tropopause layer (Fig. 11b) and have a more comparable power at most scales.

The shape of the Kelvin E_D^k spectra is similar to the WIG and EIG spectra as could be expected based on the same frequency-zonal wavenumber, $\nu - k$, scaling. But, the Kelvin E_D^k amplitude is 1-2 orders of magnitude smaller power compared to EIG modes. The power in both IG and Kelvin waves drops sharply beyond $k \approx 100$ which is most likely due to the insufficient ERA5 model resolution. The MRG and Rossby E_D^k spectra are very steep beyond planetary and large synoptic scales which is expected given their $\nu - k$ scaling. The MRG waves in August 2018 had a comparable signal to the Kelvin E_D^k only at planetary scales and more so in the tropopause layer.

Why there is relatively little divergence in the Kelvin and MRG waves compared to IG modes? The answer lies in their particular nature of being a scale-dependent mixture of divergent and rotational flow. The Hough decomposition followed by the Helmholtz decomposition can quantify the divergent and rotational potions of the Kelvin and MRG kinetic energies as a function of the zonal wavenumber (Eq. 13). Its application to our August 2018 data is shown in Fig. 12. At $k = 1$, the Kelvin wave is predominantly rotational (Fig. 12a), similar to its climatological spectrum (Žagar et al., 2022). The divergent energy becomes dominant for $k > 2$ and makes most of the kinetic energy at subsynoptic scales. The total and divergent Kelvin wave kinetic energy spectrum is some-

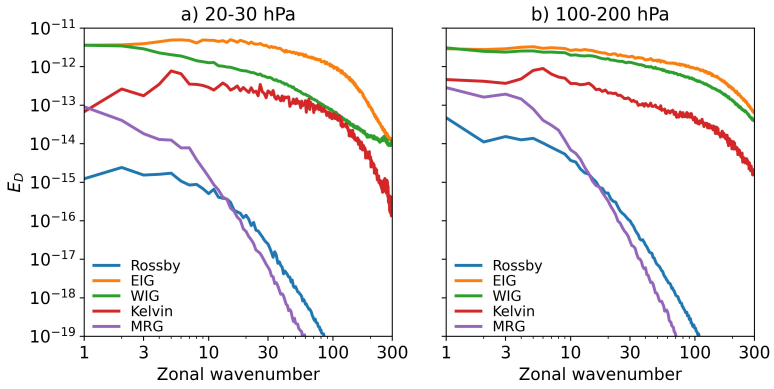

Figure 11. Divergence power spectra E_D^k averaged for latitudes 10°N−10°S and a) 20-30 hPa, b) 100-200 hPa layers. E_D^k is evaluated separately for the Rossby (R), EIG, WIG, Kelvin (K), and MRG waves.

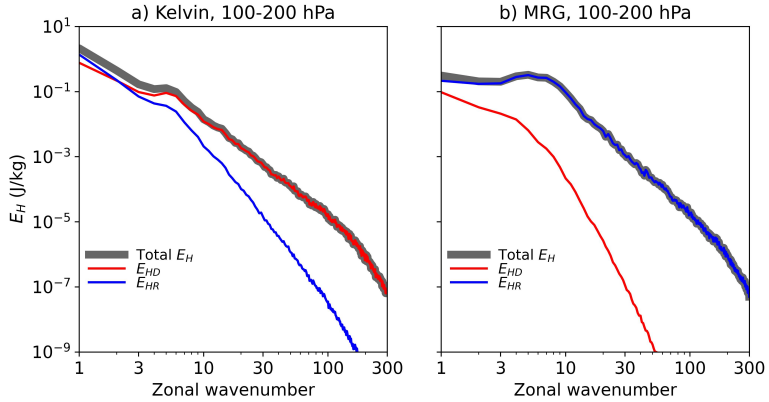

Figure 12. The horizontal kinetic energy spectra of the a) Kelvin and b) MRG waves averaged for levels between 100 and 200 hPa for August 2018 ERA5 data. The total kinetic energy E_H is split between the divergent, E_{HD}, and rotational, E_{HR}, parts. See the text for details.

what shallower than a k^{-3} power law. The MRG waves within the 100-200 hPa layer are characterised by negligible divergent kinetic energy beyond planetary scales. The total and rotational kinetic energy spectra of the MRG waves follow a k^{-3} power law similar to the Rossby waves (not shown). This explains an almost negligible MRG E_D^k signal in Fig. 9 outside large scales.

Finally, we show in Fig. 13 the E_D^k spectra for the subtropical belts of both hemispheres that complement the physical picture discussed for other latitudes. The largest difference compared to other regions is between EIG and Rossby modes for the NH and SH subtropics. The EIG E_D^k is stronger in NH than in SH, especially at subsynoptic scales in the upper stratosphere (Fig. 13b vs. Fig. 13e). This may be associated with stronger gravity wave activity in the monsoon latitudes. Compared to midlatitude spectra (Fig. 6), the IG E_D^k in the upper troposphere is more significant at planetary scales, like in the tropics. This is to a small extent also related to the Kelvin and MRG signals extending beyond 10° away from the equator (Fig. 13h,i,k,l). The meridional half-scale of both waves is known to be 5°-10° in the troposphere but grows significantly greater in the upper troposphere (e.g., Knippertz et al., 2022; Yang et al., 2023) and mesosphere (e.g., Garcia

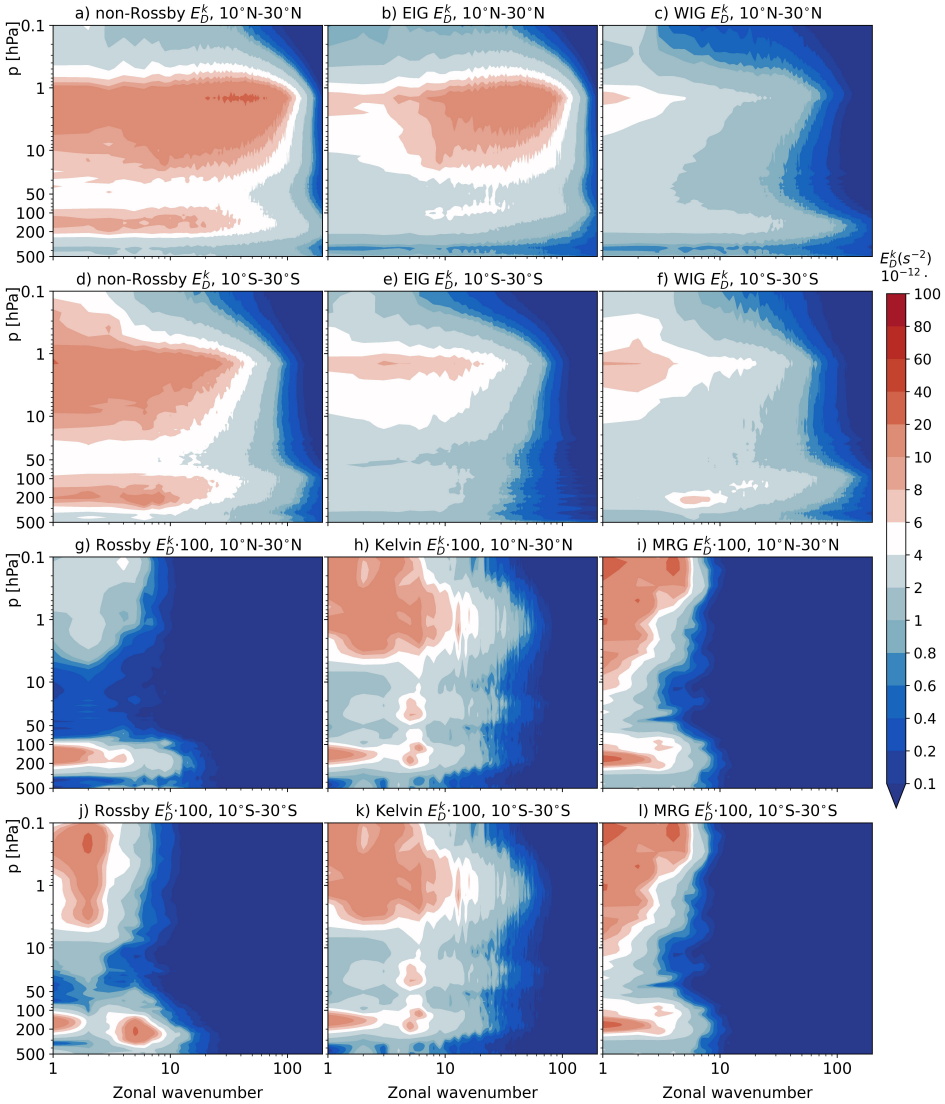

Figure 13. As in Fig. 9 but for the latitude belt (a-c and g-i) 10°N-30°N and (d-f and j-l) 10°S-30°S. The Rossby, Kelvin, and MRG divergence spectra are multiplied by 100. Note the nonlinear contour intervals.

et al., 2005). The Kelvin wave and MRG wave meridional scales in the real-time ECMWF analyses and forecasts can be seen at `https://modes.cen.uni-hamburg.de/products#KW` and `https://modes.cen.uni-hamburg.de/products#MRG`, respectively. It can be noticed in Fig. 13 that the Kelvin E_D^k is relatively smaller than the MRG E_D^k compared to the 10^0S-10^0N belt which is because the Kelvin wave divergence is centered at the equator whereas the MRG wave divergence is largest away from the equator (see Fig. 1). At subsynoptic scales in the summer (NH) subtropical stratosphere, the EIG E_D^k makes over 80% of the total divergent power. It is the opposite in the upper troposphere and tropopause layers, where the WIG modes contain the majority of divergence power in subtropical SH (not shown). Both properties are easily associated with the season and the background flow. Finally, the Rossby mode divergence power in August 2018 has its global maximum between 300 and 200 hPa levels in SH subtropics (not shown).

4 Discussion and Conclusions

This paper extended the application of the linear normal-mode decomposition to divergence, as a key intermediate step towards a unified decomposition of the vertical velocity (Žagar et al., 2023) and the vertical momentum fluxes that remain an order one challenge for weather and climate models (e.g., Geller et al., 2013), even for km-scale models (e.g., Polichtchouk et al., 2022). An important novel aspect of our approach is the co-existence of the tropical Rossby, IG, Kelvin and MRG waves at the same zonal scales and implicitly also at the same frequencies.

It has long been established that subsynoptic scales of motions largely project onto IG modes (e.g., Tanaka & Žagar, 2020, and references therein). Žagar et al. (2009b, 2009a) demonstrated that filtering IG modes back to physical space produces physically informative horizontal winds, geopotential height and temperature perturbations associated with Rossby and IG waves, and equatorial waves in particular. Scale-selective filtering of IG modes shows that divergence-dominated flows span the scales from the mean-zonal state (i.e. Hadley cell) (Puri, 1983; Pikovnik et al., 2022) to large-scale waves (Puri, 1988; Žagar et al., 2009a) and smaller-scale coherent structures. The latter are more difficult to identify as waves within the tropical troposphere because of their coupling with convection, with the nonlinear coupling represented by smaller equivalent depths (i.e. wave speeds) compared to the values for the dry waves (e.g., Kiladis et al., 2009; Knippertz et al., 2022). The 3D normal-mode decomposition couples the vertical structure of waves and their horizontal properties through the equivalent depths. Multiple depths or VSFs are involved in the representation of wave signals within various layers and not every small-scale structure projecting on IG modes is a wave in the sense that its phase speed and energy propagation can be diagnosed for example by the hodograph method (Hamilton, 1991; Sato & Yamada, 1994; Fritts & Alexander, 2003). On the other hand, this is easily demonstrated for large-scale waves such as the Kelvin wave (Žagar et al., 2009a), and for extratropical stratospheric gravity waves (Dörnbrack et al., 2018). Furthermore, Žagar et al. (2017) demonstrated by the hodograph method that also tropospheric extratropical gravity waves can be filtered out using the NMF decomposition.

In this paper, we focused on scales from hundreds of km to synoptic and planetary wavenumbers which are commonly identified as most relevant for equatorial waves. Presented divergence power spectra reflect physical properties of the flow, some of which have been well established, primarily in the extratropics. In particular, even though we perform the wavenumber decomposition that does not explicitly account for wave propagation, i.e for their frequencies and the effects of the vertical variations of the large-scale background wind through which the waves propagate, the spectral distribution of IG divergence in extratropics and throughout the middle atmosphere is easily explained by considering effects of the background wind.

The key new result of this study concerns the decomposition of divergence and divergence power in the tropics. This is enabled by a new method that provides divergence as a function of the pressure level and latitude. In order to quantify the divergence power in various wave species, we compare in Fig. 14 portions of the zonally-integrated divergence power of different waves within seven latitude belts. To make the discussion of vertically-varying E_D^k easier, the zonal-mean zonal wind profile and its vertical shear are added.

Focusing first on the tropical distributions (red lines in panels a) to e) of Fig. 14), we can see that the Kelvin waves make 4-6% of the total divergent power in the tropical troposphere with a maximum around 150 hPa, where the Kelvin wave signal is strongest (Žagar et al., 2022). The tropical MRG wave portion of E_D^k in the troposphere is up to 0.5% or an order of magnitude smaller than for the Kelvin waves. An approximate estimate of divergence portions is given by the square roots of power implying about 20% and about 7% of divergence associated with the Kelvin and MRG waves in tropical belt 10^0S-10^0N (as square roots of 0.05 and 0.005 for the Kelvin and MRG waves, respectively).

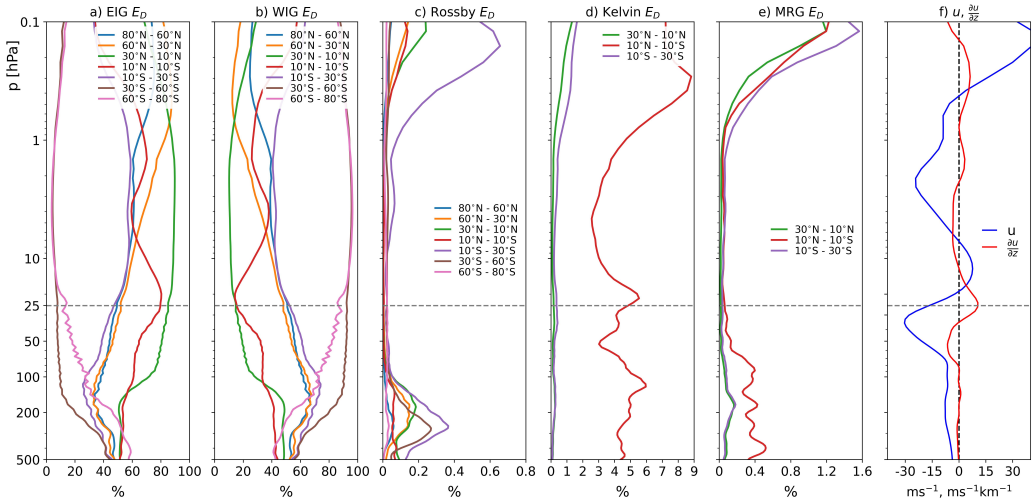

Figure 14. Vertical profiles of the relative contributions of the a) EIG, b) WIG, c) Rossby, d) Kelvin, and e) MRG divergence power zonally integrated for $k = 1 - 100$ within different latitude belts. f) Vertical profile of the zonal-mean zonal wind and its vertical shear in the tropical belt 10^0S-10^0N. Dashed line represents the level of the maximal shear.

These percentages can grow much larger in some wave numbers. In August 2018, the Kelvin wave power was up to 24% at several synoptic scales implying almost 50% of the horizontal wind divergence due to the Kelvin waves at these scales. Similarly, 10% of the divergent power due to MRG waves at planetary scales in the tropopause in August 2018 implies about 1/3 of the horizontal wind divergence at these wavenumbers. Together, the two waves made up to 6% of the zonally-integrated divergence power (E_D) in August 2018 which is about 25% of divergence. At selected wavenumber, these percentages grow much larger calling for studies of longer datasets in reanalyses and climate models and of temporal variance of E_D. While longer datasets are yet to be analysed, our results advise against using divergence as a proxy for the Kelvin waves. The results also support small amplitudes of the MRG waves reported by Lu et al. (2020) as realistic to the extent of the realism of reanalysis data. The relatively small roles of the Kelvin and MRG waves in tropical divergence are explained by comparing their rotational and divergent kinetic energy spectra. The MRG waves at all scales and $k = 1$ Kelvin wave are predominantly rotational in the upper tropical troposphere. Although divergence above 1 hPa in ERA5 is not trustworthy, we note a growing portion of the MRG and Kelvin wave divergence power above 1 hPa (Fig. 14d,e), with the MRG maximum just above the peak westerly flows near 0.2 hPa.

The majority of non-Rossby divergence is approximately equally distributed between the EIG and WIG modes in the tropical troposphere whereas the stratospheric partitioning depends on the background flow and its shear (Fig. 14a,b). In the extratropics, over 90% divergence power above 150 hPa in the winter hemisphere (SH in August 2018) is associated with WIG modes, and the same applies to EIG modes in the summer hemisphere (NH). Finally, the Rossby wave divergence power is below 0.4% implying up to 6% of global divergence due to the beta effect (the geostrophic wind divergence on the sphere, $-v_g f/\beta$). The E_D of 0.3-0.4% peaks near 300 hPa in winter associated with synoptic-scale baroclinic waves and jets that are known to be stronger in the winter hemisphere. In summer hemisphere extratropics, the Rossby wave divergence peak makes about 0.2% of E_D near 200 hPa (Fig. 14c).

Data Availability Statement

The ERA5 data were obtained from Copernicus Climate Change Service (C3S, 2017), downloaded in March 2021. Hough expansion coefficients of ERA5 input fields and Fourier coefficients of divergence associated with different wave types can be found publicly available at `https://doi.org/10.5281/zenodo.10080436` (Neduhal, 2023). The default version of the MODES software is available via `http://modes.cen.uni-hamburg.de`. Figures were made with Matplotlib version 3.2.1 (Hunter, 2007), available under the Matplotlib license at `https://matplotlib.org/`.

Acknowledgments

This paper is a contribution to the Collaborative Research Centre TRR 181 "Energy Transfers in Atmosphere and Ocean" funded by the Deutsche Forschungsgemeinschaft (DFG, German Research Foundation), project no. 274762653. Ž. Zaplotnik was supported by the Slovenian Research Agency (ARRS), grant no. J1-9431 and Program P1-0188. We thank Sergiy Vasylkevych and Richard Blender for the discussions.

References

Adams, J. C., & Swarztrauber, P. N. (2001). SPHEREPACK 3.0: A model development facility. *Mon. Wea. Rev.*, *127*, 1872–1878. doi: https://doi.org/10.1080/16000870.2016.1271563

Baldwin, M. P., Gray, L. J., Dunkerton, T. J., Hamilton, K., Haynes, P. H., Randel, W. J., ... M, T. (2001). The quasi-biennial oscillation. *Rev. Geophys.*, *39*(2), 179-229. doi: https://doi.org/10.1080/16000870.2016.1271563

Banacos, P. C., & Schultz, D. M. (2005). The use of moisture flux convergence in forecasting convective initiation: Historical and operational perspectives. *Weather and Forecasting*, *20*(3), 351–366. doi: https://doi.org/10.1175/WAF858.1

Berry, G., & Reeder, M. J. (2014). Objective identification of the intertropical convergence zone: Climatology and trends from the era-interim. *J. Clim.*, *27*(5), 1894–1909. doi: https://doi.org/10.1175/JCLI-D-13-00339.1

Bley, S., Rennie, M., Žagar, N., Pinol Sole, M., Straume, A. G., Antifaev, J., ... others (2022). Validation of the aeolus l2b rayleigh winds and ecmwf short-range forecasts in the upper troposphere and lower stratosphere using loon super pressure balloon observations. *Q. J. R. Meteorol. Soc.*, *148*(749), 3852–3868. doi: https://doi.org/10.1002/qj.4391

Bony, S., & Stevens, B. (2019). Measuring area-averaged vertical motions with dropsondes. *J. Atmos. Sci.*, *76*(3), 767–783. doi: https://doi.org/10.1175/JAS-D-18-0141.1

Bony, S., Stevens, B., Ament, F., Bigorre, S., Chazette, P., Crewell, S., ... others (2017). Eurec4a: A field campaign to elucidate the couplings between clouds, convection and circulation. *Surv. Geophys.*, *38*, 1529–1568. doi: https://doi.org/10.1007/s10712-017-9428-0

Burgess, B. H., Erler, A. R., & Shepherd, T. G. (2013). The troposphere-to-stratosphere transition in kinetic energy specra and nonlinear spectral fluxes as seen in ECMWF analyses. *J. Atmos. Sci.*, *70*(2), 669–687. doi: https://doi.org/10.1175/JAS-D-12-0129.1

C3S. (2017). *ERA5: Fifth generation of ECMWF atmospheric reanalyses of the global climate. Accessed on Mar-2021.* [dataset]. Retrieved from `https://cds.climate.copernicus.eu/#!/home`

Charney, J. G., & Drazin, P. G. (1961). Propagation of planetary scale disturbances from the lower into the upper atmosphere. *J. Geophys. Res.*, *66*, 83–109. doi: https://doi.org/10.1029/JZ066i001p00083

Dai, A., & Deser, C. (1999). Diurnal and semidiurnal variations in global surface

wind and divergence fields. *J. Geophys. Res.*, *104*(D24), 30853–31809. doi: https://doi.org/10.1029/1999JD900927

Dörnbrack, A., Bechtold, P., & Schumann, U. (2022). High-resolution aircraft observations of turbulence and waves in the free atmosphere and comparison with global model predictions. *J. Geophys. Res. Atmos.*, *127*(16), e2022JD036654. doi: https://doi.org/10.1029/2022JD036654

Dörnbrack, A., Gisinger, S., Kaifler, N., Portele, T., Bramberger, M., Rapp, M., ... Jelić, D. (2018). Gravity waves excited during a minor sudden stratospheric warming. *Atmos. Chem. Phy.*, *18*(17), 12915–12931. doi: https://doi.org/10.5194/acp-18-12915-2018

Ern, M., & Preusse, P. (2009). Wave fluxes of equatorial Kelvin waves and QBO zonal wind forcing derived from SABER and ECMWF temperature space-time spectra. *Atmos. Chem. Phys.*, *9*, 3957–3986. doi: https://doi.org/10.5194/acp-9-3957-2009

Fritts, D. C., & Alexander, J. M. (2003). Gravity wave dynamics and effects in the middle atmosphere. *Rev. Geophys.*, *41*(1). doi: https://doi.org/10.1029/2001RG000106

Garcia, R. R., Lieberman, R., Russell, J. M., & Mlynczak, M. G. (2005). Large-scale waves in the mesosphere and lower thermosphere observed by SABER. *J. Atmos. Sci.*, *62*(12), 4384–4399. doi: https://doi.org/10.1175/JAS3612.1

Geller, M. A., Alexander, M. J., Love, P. T., Bacmeister, J., Ern, M., Hertzog, A., ... Zhou, T. (2013). A comparison between gravity wave momentum fluxes in observations and climate models. *J. Climate*, *26*(17), 6383–6405. doi: https://doi.org/10.1175/JCLI-D-12-00545.1

Gill, A. E. (1980). Some simple solution for heat-induced tropical circulation. *Q. J. R. Meteorol. Soc.*, *106*(449), 447–462. doi: https://doi.org/10.1002/qj.49710644905

Gisinger, S., Polichtchouk, I., Dörnbrack, A., Reichert, R., Kaifler, B., Kaifler, N., ... Sandu, I. (2022). Gravity-wave-driven seasonal variability of temperature differences between ecmwf ifs and rayleigh lidar measurements in the lee of the southern andes. *J. Geophys. Res. Atmos.*, *127*(13), e2021JD036270. doi: https://doi.org/10.1029/2021JD036270

Gupta, A., Birner, T., Dörnbrack, A., & Polichtchouk, I. (2021). Importance of gravity wave forcing for springtime southern polar vortex breakdown as revealed by era5. *Geophys. Res. Lett.*, *48*(10), e2021GL092762. doi: https://doi.org/10.1029/2021GL092762

Hamilton, K. (1991). Climatological statistics of stratospheric inertia-gravity waves deduced from historical rocketsonde wind and temperature data. *J. Geophys. Res*, *96*(20), 831–20. doi: https://doi.org/10.1029/91JD02188

Hersbach, H., Bell, B., Berrisford, P., Hirahara, S., Horányi, A., Muñoz-Sabater, J., ... Thépaut, J.-N. (2020). The era5 global reanalysis. *Q. J. R. Meteorol. Soc.*, *146*(730), 1999–2049. doi: https://doi.org/10.1002/qj.3803

Holton, J. R. (2004). *An introduction to dynamic meteorology* (4th ed.; R. Dmowska & J. R. Holton, Eds.). Burlington, MA: Elsevier Academic Press,.

Hunter, J. D. (2007). Matplotlib: A 2d graphics environment. *Computing in Science & Engineering*, *9*(3), 90–95. doi: https://doi.org/10.1109/MCSE.2007.55

Jakobsen, F., & Madsen, H. (2004). Comparison and further development of parametric tropical cyclone models for storm surge modelling. *J. Wind. Eng. Ind. Aerodyn.*, *92*(5), 375–391. doi: https://doi.org/10.1016/j.jweia.2004.01.003

Kasahara, A. (2020). 3d normal mode functions (nmfs) of a global baroclinic atmospheric model. In N. Žagar & J. Tribbia (Eds.), *Modal view of atmospheric variability: Applications of normal-mode function decomposition in weather and climate research* (pp. 1–61). Cham: Springer International Publishing. doi: https://doi.org/10.1007/978-3-030-60963-4_1

Kiladis, G. N., Dias, J., & Gehne, M. (2016). The Relationship between Equatorial

Mixed Rossby–Gravity and Eastward Inertio-Gravity Waves. Part I. *J. Atmos. Sci.*, *73*(5), 2123–2145. doi: https://doi.org/10.1175/JAS-D-15-0230.1

Kiladis, G. N., Wheeler, M. C., Haertel, P. T., Straub, K. H., & Roundy, P. E. (2009). Convectively coupled equatorial waves. *Rev. Geophys.*, *47*(2). doi: https://doi.org/10.1029/2008RG000266

Kim, Y.-H., & Chun, H.-Y. (2015). Contributions of equatorial wave modes and parameterized gravity waves to the tropical QBO in HadGEM2. *J. Geophys. Res. Atmos.*, *120*(3), 1065–1090. doi: https://doi.org/10.1002/2014JD022174

Kimberlain, T. B. (2016). *Tropical storm Fiona*. National Hurricane Center. Retrieved from `https://www.nhc.noaa.gov/data/tcr/AL062016_Fiona.pdf`

Knippertz, P., Gehne, M., Kiladis, G. N., Kikuchi, K., Rasheeda Satheesh, A., Roundy, P. E., ... Wheeler, M. C. (2022). The intricacies of identifying equatorial waves. *Q. J. R. Meteorol. Soc.*, *148*(747), 2814–2852. doi: https://doi.org/10.1002/qj.4338

Ko, S. D., Tribbia, J. J., & Boyd, J. P. (1981). Energetics analysis of a multilevel global spectral model. Part I: Balanced energy and transient energy. *Mon. Wea. Rev.*, *117*(9), 1941-1953. doi: https://doi.org/10.1175/1520-0493(1989)117⟨1941:EAOAMG⟩2.0.CO;2

Lambert, S. J. (1984). A global available potential energy-kinetic energy budget in terms of the two-dimensional wavenumber for the FGGE year. *Atmos. - Ocean.*, *22*(3), 265–282. doi: https://doi.org/10.1080/07055900.1984.9649199

Lott, F., & Miller, M. J. (1997). A new subgrid-scale orographic drag parametrization: Its formulation and testing. *Q. J. R. Meteorol. Soc.*, *123*(537), 101–127. doi: https://doi.org/10.1002/qj.49712353704

Lu, Y., Wu, T., Jie, W., Scaife, A. A., Andrews, M. B., & Richter, J. H. (2020). Variability of the Stratospheric Quasi-Biennial Oscillation and Its Wave Forcing Simulated in the Beijing Climate Center Atmospheric General Circulation Model. *J. Atmos. Sci.*, *77*(1), 149–165. doi: https://doi.org/10.1175/JAS-D-19-0123.1

Matsuno, T. (1966). Quasi-geostrophic motions in the equatorial area. *J. Meteor. Soc. Japan*, *44*(1), 25–42. doi: https://doi.org/10.2151/jmsj1965.44.1_25

Nappo, C. J. (2002). *An introduction to atmospheric gravity waves* (2nd ed.). Amsterdam: Academic Press, Elsevier Science.

Neduhal, V. (2023). *Decomposition of the horizontal wind divergence using modes* [dataset]. Zenodo. doi: https://doi.org/10.5281/zenodo.10080436

Orr, A., Bechtold, P., Scinocca, J., Ern, M., & Janiskova, M. (2010). Improved middle atmosphere climate and forecasts in the ECMWF model through a non-orographic gravity wave drag parametrization. *J. Climate*, *23*(22), 5905–5926. doi: https://doi.org/10.1175/2010JCLI3490.1

O'Sullivan, D., & Dunkerton, T. J. (1995). Generation of inertia–gravity waves in a simulated life cycle of baroclinic instability. *J. Atmos. Sci.*, *52*(21), 3695–3716. doi: https://doi.org/10.1175/1520-0469(1995)052⟨3695:GOIWIA⟩2.0.CO;2

Pikovnik, M., Zaplotnik, v., Boljka, L., & Žagar, N. (2022). Metrics of the hadley circulation strength and associated circulation trends. *Weather Clim. Dynam*, *3*(2), 625–644. doi: https://doi.org/10.5194/wcd-3-625-2022

Plougonven, R., & Zhang, F. (2014). Internal gravity waves from atmospheric jets and fronts. *Rev. Geophys.*, *52*(1), 33–76. doi: https://doi.org/10.1002/2012RG000419

Polichtchouk, I., Van Niekerk, A., & Wedi, N. (2023). Resolved Gravity Waves in the Extratropical Stratosphere: Effect of Horizontal Resolution Increase from O (10) to O (1) km. *J. Atmos. Sci.*, *80*(2), 473–486. doi: https://doi.org/10.1175/JAS-D-22-0138.1

Polichtchouk, I., Wedi, N., & Kim, Y.-H. (2022). Resolved gravity waves in the tropical stratosphere: Impact of horizontal resolution and deep convection parametrization. *Q. J. R. Meteorol. Soc.*, *148*(742), 233–251. doi:

https://doi.org/10.1002/qj.4202

Puri, K. (1983). The relationship between convective adjustment Hadley circulation and normal modes of the ANMRC spectral model. *Mon. Wea. Rev.*, *111*(1), 23–33. doi: https://doi.org/10.1175/1520-0493(1983)111⟨0023:TRBCAH⟩2.0.CO;2

Puri, K. (1988). On the importance of low-frequency gravity modes for the evolution of large-scale flow in a general circulation model. *J. Atmos. Sci.*, *45*(18), 2523–2544. doi: https://doi.org/10.1175/1520-0469(1988)045⟨2523:OTIOLF⟩2.0.CO;2

Rennie, M. P., Isaksen, L., Weiler, F., de Kloe, J., Kanitz, T., & Reitebuch, O. (2021). The impact of Aeolus wind retrievals on ECMWF global weather forecasts. *Q. J. R. Meteorol. Soc.*, *147*(740), 3555–3586. doi: https://doi.org/10.1002/qj.4142

Sato, K., & Yamada, M. (1994). Vertical structure of atmospheric gravity waves revealed by the wavelet analysis. *J. Geophys. Res. Atmos.*, *99*(D10), 20623–20631. doi: https://doi.org/10.1029/94JD01818

Savazzi, A. C. M., Nuijens, L., Sandu, I., George, G., & Bechtold, P. (2022). The representation of the trade winds in ECMWF forecasts and reanalyses during EUREC^{4}A. *Atmos. Chem. Phys.*, *22*(19), 13049–13066. doi: https://doi.org/10.5194/acp-22-13049-2022

Skamarock, W. C., Park, S.-H., Klemp, J. B., & Snyder, C. (2014). Atmospheric kinetic energy spectra from global high-resolution nonhydrostatic simulation. *J. Atmos. Sci.*, *71*(11), 4369–4381. doi: https://doi.org/10.1175/JAS-D-14-0114.1

Staniforth, A., Beland, M., & Coté, J. (1985). An analysis of the vertical structure equation in sigma coordinates. *Atmos.-Ocean*, *23*, 323–358. doi: https://doi.org/10.1080/07055900.1985.9649232

Stoffelen, A., Pailleux, J., Källén, E., Vaughan, J. M., Isaksen, L., Flamant, P., ... Ingmann, P. (2005). The atmospheric dynamic mission for global wind measurements. *Bull. Amer. Meteor. Soc.*, *86*(1), 73–87. doi: https://doi.org/10.1175/BAMS-86-1-73

Swarztrauber, P. N., & Kasahara, A. (1985). The vector harmonic analysis of laplace tidal equations. *SIAM J. Stat. Comput.*, *6*(2), 464–491. doi: https://doi.org/10.1137/0906033

Tanaka, H., & Žagar, N. (2020). 3d modal variability and energy transformations on the sphere. In N. Žagar & J. Tribbia (Eds.), *Modal view of atmospheric variability: Applications of normal-mode function decomposition in weather and climate research* (pp. 121–179). Cham: Springer International Publishing. doi: https://doi.org/10.1007/978-3-030-60963-4_1

Terasaki, K., Tanaka, H., & Žagar, N. (2011). Energy spectra of Rossby and gravity waves. *SOLA*, *7*(1), 45–48. doi: https://doi.org/10.2151/sola.2011-012

Trenberth, K. E., Stepaniak, D. P., & Caron, J. M. (2000). The global monsoon as seen through the divergent atmospheric circulation. *J. Climate*, *13*, 3969–3993. doi: https://doi.org/10.1175/1520-0442(2000)013⟨3969:TGMAST⟩2.0.CO;2

Tribbia, J. (2020). Normal Mode Functions and Initialization. In N. Žagar & J. Tribbia (Eds.), *Modal view of atmospheric variability: Applications of normal-mode function decomposition in weather and climate research* (pp. 63–78). Cham: Springer International Publishing. doi: https://doi.org/10.1007/978-3-030-60963-4_1

Uccellini, L. W., & Koch, S. E. (1987). The synoptic settings and possible energy sources for mesoscale wave disturbances. *Mon. Wea. Rev.*, *115*(3), 721–729. doi: https://doi.org/10.1175/1520-0493(1987)115⟨0721:TSSAPE⟩2.0.CO;2

Žagar, N., Jelić, D., Blaauw, M., & Bechtold, P. (2017). Energy spectra and inertia-gravity waves in global analyses. *J. Atmos. Sci.*, *74*, 2447–2466. doi: https://doi.org/10.1175/JAS-D-16-0341.1

Žagar, N., Kasahara, A., Terasaki, K., Tribbia, J., & Tanaka, H. (2015). Normal-mode function representation of global 3D datasets: open-access software for the atmospheric research community. *Geosci. Model Dev.*, *8*(4), 1169–1195. doi: https://doi.org/10.5194/gmd-8-1169-2015

Žagar, N., Lunkeit, F., Sielmann, F., & Xiao, W. (2022). Three-dimensional structure of the equatorial kelvin wave: Vertical structure functions, equivalent depths, and frequency and wavenumber spectra. *J. Clim.*, *35*(7), 2209–2230. doi: https://doi.org/10.1175/JCLI-D-21-0342.1

Žagar, N., Neduhal, V., Vasylkevych, S., Ž. Zaplotnik, & Tanaka, H. (2023). Decomposition of vertical velocity and its zonal wavenumber kinetic energy spectra in the hydrostatic atmosphere. *J. Atmos. Sci.*. doi: https://doi.org/10.1175/JAS-D-23-0090.1

Žagar, N., Tribbia, J., Anderson, J. L., & Raeder, K. (2009a). Uncertainties of estimates of inertia-gravity energy in the atmosphere. Part II: large-scale equatorial waves. *Mon. Wea. Rev.*, *137*(11), 3858–3873. Corrigendum, Mon. Wea. Rev., 138, 2476-2477. doi: https://doi.org/10.1175/2009MWR2816.1

Žagar, N., Tribbia, J., Anderson, J. L., & Raeder, K. (2009b). Uncertainties of estimates of inertia-gravity energy in the atmosphere. Part I: intercomparison of four analysis datasets. *Mon. Wea. Rev.*, *137*(11), 3837–3857. Corrigendum, Mon. Wea. Rev., 138, 2476-2477. doi: https://doi.org/10.1175/2009MWR2815.1

Waite, M. L., & Snyder, C. (2009). The mesoscale kinetic energy spectrum of a baroclinic life cycle. *J. Atmos. Sci.*, *66*(4), 883–901. doi: https://doi.org/10.1175/2008JAS2829.1

Wang, C. (2002). Atmospheric circulation cells associated with the El Nino-Southern Oscillation. *J. Clim.*, *15*(4), 399–419. doi: https://doi.org/10.1175/1520-0442(2002)015⟨0399:ACCAWT⟩2.0.CO;2

Webster, P. (2020). *Dynamics of the tropical atmosphere and oceans.* Chichester, UK: John Wiley and Sons, Ltd.

Wedi, N. P. (2014). Increasing horizontal resolution in numerical weather prediction and climate simulations: illusion or panacea? *Phil. Trans. R. Soc. A*, *372*(2018). doi: https://doi.org/10.1098/rsta.2013.0289

Wheeler, M., Kiladis, G. N., & Webster, P. J. (2000). Large-scale dynamical fields associated with convectively coupled equatorial waves. *J. Atmos. Sci.*, *57*(5), 613–640. doi: https://doi.org/10.1175/1520-0469(2000)057⟨0613:LSDFAW⟩2.0.CO;2

Yang, G.-Y., Feng, X., & Hodges, K. (2023). Seasonal and interannual variation of equatorial waves in ERA5 and GloSea5. *Q. J. R. Meteorol. Soc.*, *149*(752), 1109–1134. doi: https://doi.org/10.1002/qj.4460

Yang, G.-Y., Hoskins, B. J., & Slingo, J. (2003). Convectively coupled equatorial waves: A new methodology for identifying wave structures in observational data. *J. Atmos. Sci.*, *60*, 1637–1654. doi: https://doi.org/10.1175/1520-0469(2003)060⟨1637:CCEWAN⟩2.0.CO;2

Zurita-Gotor, P. (2019). The Role of the Divergent Circulation for Large-Scale Eddy Momentum Transport in the Tropics. Part I: Observations. *J. Atmos. Sci.*, *76*(4), 1125–1144. doi: https://doi.org/10.1175/JAS-D-18-0297.1

Zurita-Gotor, P. (2021). The interannual variability of the tropical divergence tilt and its connection with the extratropical circulation. *J. Clim.*, *34*(1), 259–275. doi: https://doi.org/10.1175/JCLI-D-20-0373.1